Theor. Comput. Fluid Dyn.
https://doi.org/10.1007/s00162-023-00648-z

ORIGINAL ARTICLE

Hariharan Ramanathan · Ashok Gopalarathnam

Prediction of leading-edge-vortex initiation using criticality of the boundary layer

Received: 15 December 2022 / Accepted: 13 April 2023

Abstract The initiation of leading-edge-vortex formation in unsteady airfoil flows is governed by flow criticality at the leading edge. While earlier works demonstrated the promise of criticality of leading-edge suction in governing LEV shedding, this criterion is airfoil and Reynolds number dependent. In this work, by examining results from Navier–Stokes computations for a large set of pitching airfoil cases at laminar flow conditions, we show that the onset of flow reversal at the leading edge always corresponds to the boundary-layer shape factor reaching the same critical value that governs laminar flow separation in steady airfoil flows. Further, we show that low-order prediction of this boundary-layer criticality is possible with an integral-boundary-layer calculation performed using potential-flow velocity distributions from an unsteady panel method. The low-order predictions agree well with the high-order computational results with a single empirical offset that is shown to work for multiple airfoils. This work shows that boundary-layer criticality governs LEV initiation, and that a low-order prediction approach is capable of predicting this boundary-layer criticality and LEV initiation.

Keywords Unsteady aerodynamics · LESP · Separated flows · Boundary layer separation · Vortical flows

1 Introduction

Although leading-edge-vortex (LEV) shedding from unsteady airfoils and wings is ubiquitous in nature and engineering and has been studied for several decades, there is still much to be understood about the initiation of LEV formation and how to predict it using low-order approaches. The formation, growth, and detachment of the LEV often dominate the forces and moments on an unsteady airfoil and affect the surrounding flow fields [1–11]. It may be argued that the first step in the correct prediction of LEV effects is to be able to predict the initiation of LEV formation. On airfoils with sharp leading edges, the prediction is relatively easy as the LEV starts forming soon after the stagnation point leaves the sharp edge. On round leading edges, the flow remains attached for some time after the stagnation point moves away from the geometric leading-edge point, after which flow reversal at the leading edge precedes LEV initiation. In a pitching motion, for example, this time duration translates to a pitch angle for the LEV initiation, which ends up depending on a multitude of parameters such as pitch rate, pivot location, leading-edge shape, and Reynolds number. It has been proposed that, irrespective of the motion, leading-edge shape, and Reynolds number, LEV initiation occurs when the leading-edge flow becomes critical [12–15]. The search for a universal criticality condition for LEV initiation, however, still continues, especially for a criterion that can be easily incorporated in a low-order predictive approach. The recent development [16] and refinement [17] of the criticality of the leading-edge suction parameter (LESP)

Communicated by Karen Mulleners.

H. Ramanathan · A. Gopalarathnam (✉)
Department of Mechanical and Aerospace Engineering, North Carolina State University, Raleigh, NC 27695, USA
E-mail: hramana@ncsu.edu; agopalar@ncsu.edu

Published online: 13 May 2023

have shown some promise in being able to predict LEV initiation for a given airfoil and Reynolds number while being largely motion independent. However, the critical LESP depends on the airfoil and Reynolds number, and, for each combination, the approach requires at least one high-fidelity computational or experimental result to determine this critical LESP. Here, we study the use of boundary-layer growth on pitching round-leading-edge airfoils to explore if criticality of the leading-edge boundary layer can be connected to LEV initiation, and whether this criticality will be independent of not only motion kinematics, but also leading-edge shape and Reynolds number. An important motivation is to find a boundary-layer parameter that can be predicted using a low-order approach.

Much of the early work in LEV initiation and shedding was spurred by the need to understand and model the dynamic stall phenomenon on rotorcraft [18–20]. More recent interest over the past 15 years, on the other hand, has been motivated by research in low-Reynolds-number applications and bio-inspired flapping flight [21–26]. The LESP criterion provided a path forward for prediction of LEV initiation on round-leading-edge geometries in both two- and three-dimensional flows. An advantage of the LESP is that it is closely connected to the value at the leading edge of the bound-vortex-sheet strength used in theoretical models of unsteady airfoils and wings. However, because of the dependence of the critical LESP on airfoil shape and Reynolds number, it is worth searching for a flow parameter that avoid these dependencies. Because LEV initiation is closely connected to the onset of boundary-layer separation at the leading edge, it is natural to explore the use of a newer criterion that uses criticality of the leading-edge boundary layer. In recent years, several efforts have studied the efficacy of LESP and various extensions of that criterion [27–29]. Other research efforts have also explored the use of alternate approaches including criteria that involve boundary-layer quantities [30–34]. Deparday and Mulleners [30] showed that there is a connection between the value of the shear-layer height at the leading edge and LEV initiation. That parameter, however, depends on the availability of CFD or experimental results and is not easily calculated in a low-order formulation. In another recent work, Sudharsan and Sharma [33] connected the boundary enstrophy flux (BEF) with LEV initiation. In the current stage of development, this BEF parameter also requires detailed computational results and is not suited to incorporation in low-order prediction approaches.

There is a long history of critical values of various boundary-layer shape factors being used to predict onset of flow separation in both laminar and turbulent steady boundary layers, for example, in Refs. [35–38]. The concept of vanishing shear stress being classified as separation by Prandtl [39] works well with steady flows due to the separation point being fixed. In unsteady flow, however, boundary-layer separation is more complicated because of the movement of the separation location. Although some requirements for the flow at the unsteady separation point have been proposed [40–45], and calculation methods have been developed for unsteady boundary layers [46–48], they are more challenging than for steady flows. Fortunately, as shown by McDonald and Shamroth [49], for the flows associated with unsteady airfoils of interest in many practical dynamic stall situations, accurate prediction of the unsteady boundary-layer development can be obtained from steady-state boundary-layer theory using the velocity distribution imposed by the unsteady flow. This was recently reaffirmed by the work of Smith and Jones [31] in which they used scaling analysis for pitching and surging airfoils to show that unsteady boundary-layer effects would be negligible in predicting the onset of vortex formation for motion rates similar to those being considered in this work. Thus, it appears promising that a quasi-steady low-order approach could be developed in which the velocity distribution from an unsteady potential-flow method is used as an input in a steady integral-boundary-layer calculation to calculate the onset of separation. This idea was pursued even back in 1998 by Jones and Platzer [50] in which they used an unsteady panel method and a steady boundary-layer code to calculate the onset of dynamic stall. The motions analyzed were confined to high Reynolds number and low-pitch rate motions ($k \leq 0.1$). The pitch-angle predictions for the onset of leading-edge separation were made using the boundary-layer code with the assumption that LEV formation occurs at a location within 10% of the chord.

There are two obvious drawbacks to such a quasi-steady approach. First, the potential-flow pressure distribution does not take into consideration the "decambering effect" of the thick and/or separated boundary layers on the aft part of the airfoil. Second, it is not possible to carry out these boundary-layer calculations beyond the first occurrence of flow reversal. The first drawback could be mitigated in future by one of several approaches: incorporation of viscous–inviscid interaction [36,51], use of semiempirical means for modeling the unsteady decambering effect [52–54], or by applying an empirical correction to the results. The second drawback can be mitigated to some extent by using an unsteady boundary-layer calculation [46,47], which will allow the calculations to proceed beyond the first occurrence of flow reversal to the point of unsteady separation, as done by Paturle et al. [48].

With the acknowledgement of these advantages and limitations, our work adopts this overall idea and explores the use of such a quasi-steady approach for prediction of LEV initiation. This work is restricted to low Reynolds number of approximately 10,000, at which the boundary layer on the airfoil surface is predicted to be laminar for the shapes considered in this work. This restriction avoids the difficulty with having to model boundary-layer transition and its effects. The two main goals of this work are to: (i) verify the main hypothesis in this paper that there is a critical boundary-layer parameter that can be associated with LEV initiation for a range of kinematics, leading-edge shapes, Reynolds numbers, and airfoil geometries and (ii) to study the use of a low-order approach that uses this boundary-layer criticality in predicting LEV initiation on unsteady airfoils without the explicit need for a high-order computation. Preliminary results from authors' efforts were presented in Refs. [55] and [56], which addressed the first and second goals, respectively. In the current article, following the presentation of some essential background material on LESP and LEV initiation in Sect. 2 and a description of the unsteady motions in Sect. 3, we present the first part of the research approach in Sect. 4 in which boundary-layer information extracted from RANS CFD results for a large number of pitching-airfoil cases are used to address the first research goal of finding a boundary-layer parameter, the criticality of which is connected with LEV initiation. Section 5 then presents the second part of the research approach in which a low-order approach is developed to predict LEV initiation using this boundary-layer parameter. The results for multiple motions and geometry variations are then presented in Sect. 6 for two airfoils to show the generality of the findings and the effectiveness of the prediction approach.

2 Background

2.1 Leading-edge suction parameter (LESP)

Inspired by earlier works on flow criticality at the leading edge, Ramesh et al. [16] showed that the onset of separation at the leading edge is governed by criticality of the chordwise suction force. This chordwise force in its non-dimensional form is referred as leading edge suction parameter (LESP, denoted by $\mathcal{L}$). This parameter was later implemented as part of a theoretical formulation wherein the bound-vortex-sheet strength $\gamma(x, t)$ is represented by a Fourier series:

$$\gamma(\theta, t) = 2U_{\mathrm{ref}}\left[A_0(t)\frac{1+\cos\theta}{\sin\theta} + \sum_{n=1}^{\infty} A_n(t)\sin(n\theta)\right], \tag{1}$$

where θ represents the angular coordinate, given by $\theta = (c/2)(1 - \cos\theta)$, and $A_0(t)$, $A_1(t)$, …, $A_n(t)$ are the time-dependent Fourier coefficients. The instantaneous value of the LESP, denoted by $\mathcal{L}$, can be connected to the flow velocity at the leading-edge (V_{LE}), as shown by Ramesh [57], and this can be correlated with the circulation at leading edge which is represented by the A_0 coefficient in Eqn. 1. Based on this knowledge, the instantaneous $\mathcal{L}$ that is computed from theory, also referred as $\mathcal{L}_{\mathrm{ref}}$, is set equal to A_0,

$$\mathcal{L}_{\mathrm{ref}}(t) = A_0(t) \tag{2}$$

The subscript ref is used to denote that this $\mathcal{L}$ was computed based on the single reference velocity U_{ref}. Subsequent work by Narsipur et al. [17] proposed an alteration to the above formulation which accounts for the additional velocities resulting from high-pitch-rate motions which uses a net velocity denoted as U_{net}. The ratio $U_{\mathrm{net}}/U_{\mathrm{ref}}$ is expressed as:

$$\frac{U_{\mathrm{net}}(t)}{U_{\mathrm{ref}}} = \sqrt{\left[\frac{U(t)}{U_{\mathrm{ref}}} + \frac{\dot{\alpha}(t)c}{U_{\mathrm{ref}}}\left(\frac{1}{2} - \frac{x_p}{c}\right)\sin\alpha(t)\right]^2 + \left[\frac{\dot{h}(t)}{U_{\mathrm{ref}}} - \frac{\dot{\alpha}(t)c}{U_{\mathrm{ref}}}\left(\frac{1}{2} - \frac{x_p}{c}\right)\cos\alpha(t)\right]^2} \tag{3}$$

In the current work, $U_{\mathrm{ref}} = U$ and $U(t)$ is a constant. Using the above formulation, the definition of $\mathcal{L}$ is updated as follows:

$$\mathcal{L}_{\mathrm{net}}(t) = \frac{\mathcal{L}_{\mathrm{ref}}(t)}{(U_{\mathrm{net}}(t)/U_{\mathrm{ref}})} \tag{4}$$

For all the discussion that follows in the remainder of this paper, any reference to $\mathcal{L}$ should be understood as $\mathcal{L}_{\mathrm{net}}$.

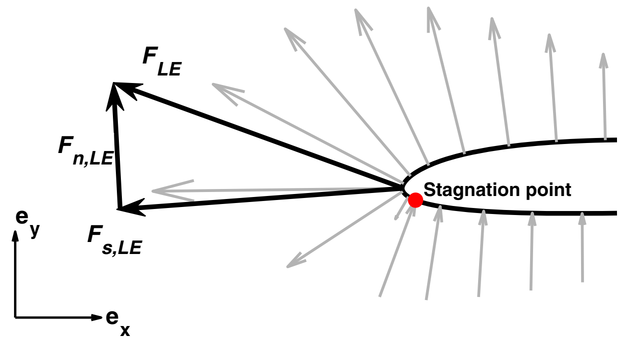

Fig. 1 Leading-edge force vector ($\vec{F}_{\mathrm{LE}}$) resolved into suction force ($\vec{F}_{s,\mathrm{LE}}$) and normal force ($\vec{F}_{n,\mathrm{LE}}$)

2.2 Critical LESP hypothesis for LEV initiation

Katz [58] proposed that airfoils with rounded leading edge support a certain amount of suction even when stagnation point is away from the leading edge. The amount of suction that can be supported is dependent on the airfoil shape and Reynolds number. Using the previous understanding that LESP is a measure of the velocity at the leading edge, the $\mathcal{L}_{\mathrm{crit}}$ hypothesis proposed by Ramesh et al. [16] is that, for a given airfoil and Reynolds number combination, the critical $\mathcal{L}$ corresponding to LEV initiation is largely independent of motion kinematics. The argument for such a thought is that for a rounded leading edge of an airfoil at a certain Reynolds number, attached flow near the leading edge is supported so long as the leading-edge suction is below a critical value. Once this critical value is exceeded, the flow at the leading edge will separate, resulting in leading-edge-vortex shedding. Although there are still small unexplained variations [17,30,59,60] of critical $\mathcal{L}$ with some motion parameters, critical $\mathcal{L}$ is largely independent of motion kinematics and is a non-dimensional measure of the suction. It therefore works as a good predictor for modeling LEV initiation on airfoils and wings in low-order formulations [28,61,62] and has also been used in studying flow-disturbance effects on unsteady airfoils [63] and unsteady motion design [64].

2.3 Determination of $\mathcal{L}$ from pressure distribution

Although the LESP is a theoretical parameter, it is of interest to extract the instantaneous value of $\mathcal{L}$ from a surface pressure distribution. This surface pressure distribution could be from a computational result or an experimental measurement. Since the $\mathcal{L}$ is a non-dimensional form of the suction force due to the leading-edge pressures, the first step is to calculate the leading-edge force, $\vec{F}_{\mathrm{LE}}$. As shown in Fig. 1, this force can be decomposed into a component along the camberline direction at the geometric leading edge, termed the "suction force," $F_{s,\mathrm{LE}}$, and a component normal to this direction, termed "normal" force, denoted by $F_{n,\mathrm{LE}}$.

From computations (CFD or panel method results), we obtain the pressure coefficient (C_p) all over the surface and integrate the C_p on all the panels over the front portion of the airfoil until some predefined distance in the chordwise direction from the leading edge. As shown in Narsipur et al. [17], to calculate the LESP, a good choice for the distance for integration ($x_{\max}/c$) is the location of maximum thickness or approximately 30% of the chord.

The net force at the leading edge and hence suction force are calculated as follows,

$$\vec{F}_{\mathrm{LE}} = q_\infty \sum_{x/c=0}^{x_{\max}/c} \left[C_p \left(\vec{\delta}_p \times \vec{e}_z \right) \right] \tag{5}$$

$$\vec{F}_s = -\left(\vec{F}_{\mathrm{LE}} \cdot \vec{e}_x \right) \vec{e}_x \tag{6}$$

where q_∞ is the dynamic pressure, $\vec{\delta}_p$ is the vector connecting the two end points of the panel for a counter-clockwise ordering of the airfoil points, and $\vec{e}_x$ and $\vec{e}_z$ are the unit vectors in the chordwise and chord-normal directions, respectively. The limit up to which panels are included in the suction force calculation is given by $x_{\max}/c$. Thus, the suction force computed in this work is the chordwise component of the net pressure force

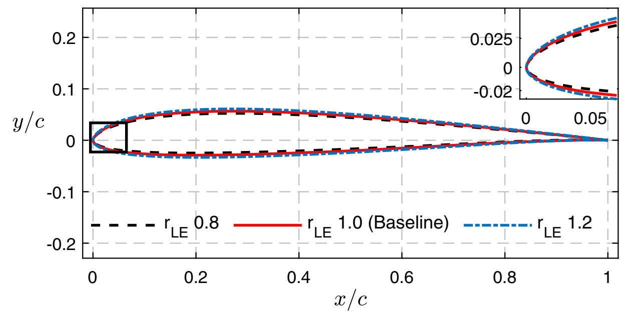

Fig. 2 Geometries of the SD7003-based airfoils used for studying the effect of leading-edge radius, r_{LE}, expressed as a ratio of the baseline-airfoil value

acting on first 30% of the airfoil. On non-dimensionalizing by the dynamic pressure and chord, the suction coefficient C_s is obtained.

$$C_s = \frac{|\vec{F}_s|}{q_\infty \, c} \tag{7}$$

The suction force coefficient, C_s, can be related to $\mathcal{L}$ using the relation in Garrick [65].

$$\mathcal{L}_{\mathrm{ref}} = \begin{cases} \mathrm{sgn}\,(C_n) \sqrt{\frac{C_s}{2\pi}}, & C_s > 0, \\ 0, & C_s \leq 0. \end{cases} \tag{8}$$

The CFD-derived/viscous suction coefficient (C_s) could sometimes be a small negative value in instances when the potential C_s is zero or a small positive value. To ensure compatibility with the potential C_s, the CFD-derived $\mathcal{L}$ is set to zero at those time instants when the viscous C_s has a negative value. Additionally, the sign of the $\mathcal{L}$ is kept the same as that of the normal force coefficient, C_n, so a positive C_n is assumed to correspond to a flow with stagnation point on the lower surface, while a negative C_n would correspond to the stagnation point being on the upper surface.

3 Cases and motion details

The pitch-up motions used in the initial part of this work use the SD7003 airfoil and its geometric derivatives. The derivatives were developed by changing the maximum t/c values using the XFOIL code [66] to effectively generate airfoils with different leading-edge radii. Figure 2 compares the two SD7003-based derivatives with the baseline SD7003 geometry. A total of 9 cases are studied to examine the boundary-layer behavior and its connection to LEV initiation. Starting with a baseline case, these cases comprise changes in the non-dimensional pitch rate ($K = \dot{\alpha}c/(2U)$, where $\dot{\alpha}$ is the pitch rate and c is the airfoil chord), pivot location, leading-edge radius (r_{LE}), and Reynolds number (Re). Pivot location is defined as the x/c location from the leading edge of the airfoil, and leading-edge radius (r_{LE}) is presented as the ratio of the leading-edge radius to that of the baseline airfoil. Table 1 lists the cases.

The same parametric variations listed in Table 1 are carried out for the NACA 0012 airfoil which is geometrically different from the SD7003 airfoil as shown in Fig. 3. The NACA 0012 has no camber and is significantly thicker (12%) as compared to the SD7003 airfoil (8.5%).

All motions are of pitch-up–hold type generated as shown in Fig. 4 using Eldredge's canonical formulation [67,68], and calculated using Eqs. 9–11.

$$\alpha = \frac{K}{a_s} \ln \left[\frac{\cosh\left(a_s\left(t^* - t_1^*\right)\right)}{\cosh\left(a_s\left(t^* - t_2^*\right)\right)} \right] + \frac{\alpha_{\mathrm{amp}}}{2} \tag{9}$$

where a_s is the smoothing parameter from Granlund et al. [68] defined as:

$$a_s = \frac{\pi^2 K}{2\alpha_{\mathrm{amp}}(1 - \sigma)} \tag{10}$$

Table 1 Cases studies using the SD7003 airfoil

Parameter	K	Pivot	r_{LE}	Re
Baseline	0.4	0.25	1.0	10,000
Pitch	**0.1**	0.25	1.0	10,000
Rate	**0.3**	0.25	1.0	10,000
Pivot	0.4	**0.0**	1.0	10,000
Location	0.4	**0.5**	1.0	10,000
Leading-edge	0.4	0.25	**0.8**	10,000
Radius	0.4	0.25	**1.2**	10,000
Reynolds	0.4	0.25	1.0	**5,000**
Number	0.4	0.25	1.0	**15,000**

Parameter change from the baseline are highlighted in bold

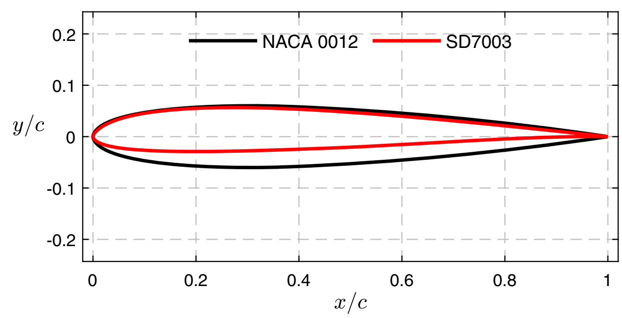

Fig. 3 Geometries of the NACA 0012 and SD7003 airfoils

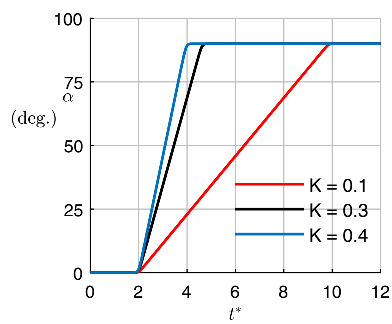

Fig. 4 Pitching kinematics

and

$$t_2^* = t_1^* + \frac{\alpha_{\text{amp}}}{2K} \tag{11}$$

In these equations, t_1^* denotes the time at start of ramp and t_2^* denotes the time at end of ramp. For all motions simulated in this paper, $t_1^* = 2$, $\alpha_{\text{amp}} = 90°$ and $a_s = 11$. The values of σ corresponding to pitch rates of $K = 0.4$, 0.3 and 0.1 are 0.88, 0.91 and 0.97, respectively.

4 CFD methodology

4.1 CFD

NCSU's REACTMB-INS solver is used for the computational fluid dynamics (CFD) calculations performed in this study. The governing equations are written in arbitrary Lagrangian/Eulerian form, which enables the motion of a body-fitted computational mesh in accord with prescribed rate laws. An incompressible version of Edwards' Low-Diffusion Flux Splitting Scheme (LDFSS) [69] is used for discretizing inviscid fluxes in space. Discretization of viscous terms is performed using a second-order central difference method. The LDFSS

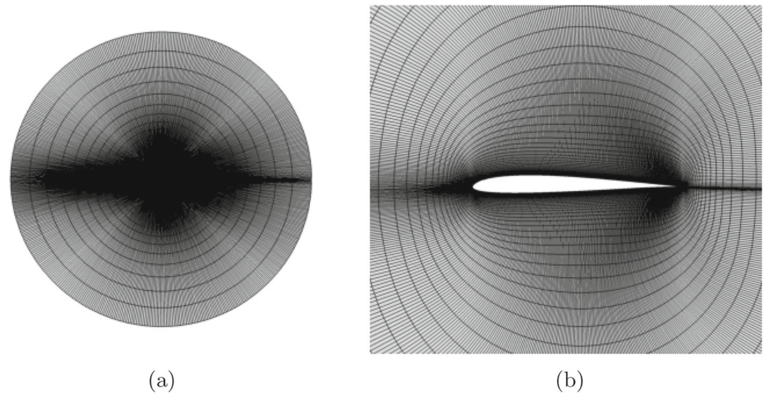

Fig. 5 Mesh topology around the airfoil

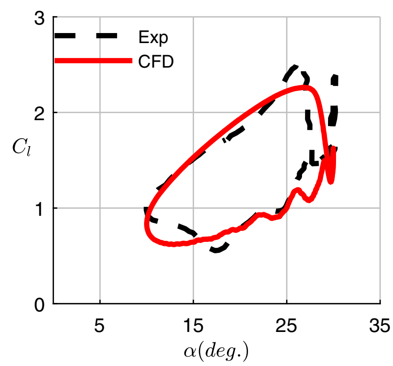

Fig. 6 Comparison of computed C_l versus α with the experimental results of Leishman [73] for the NACA 23012 airfoil at Re = 1.5 million, $k = 0.10$, $\alpha(t) = 20 + 10\sin(\omega t)$

method is extended to higher order of accuracy in space using the piecewise-parabolic method (PPM) [70]. This method is extended to higher-order spatial accuracy using PPM interpolations of the primitive variables $[p, u, v, w]^{\mathrm{T}}$ and transported variable for the S-A model, $\tilde{\nu}$. For time integration, second-order temporal accuracy is achieved by using an implicit artificial compressibility method [69] with eight subiterations at each physical time step for continuity-equation convergence. A version of Spalart–Allmaras one-equation eddy-viscosity model, modified by Edwards and Chandra [71], is used for turbulence closure.

Figure 5 shows the representative mesh distribution used in the current work. The meshes used in this investigation were generated using Pointwise$^{\mathrm{TM}}$ and contain approximately 0.15 million cells. The selected computational domain is a typical O-type grid, with its outer boundary $20c$ away from the airfoil, and structured grids are used for the whole domain. The distance of the first nodes adjacent to the airfoil surface is small enough so that the condition of $y^+ < 1$ is strictly guaranteed. A growth factor of 1.15 was used, ensuring isotropic mesh resolution in the regions close to the wall. REACTMB-INS has been extensively validated and used for incompressible and compressible flow simulations (see, e.g., Ramesh et al. [16], Hirato et al. [28], Narsipur et al. [17] and Nielsen et al. [72]).

4.2 CFD validation

Leishman [73] conducted experimental studies to examine the dynamic stall characteristics of a NACA 23012 airfoil section at a freestream Re of 1.5 million. The paper provides oscillatory pressure and force data for multiple test conditions including systematic variations of mean angle of attack, α_M, and oscillation amplitude, α_A, at different reduced frequencies (k). For our validation, we chose $\alpha_M = 20°$, with a non-dimensional pitching frequency of $k = \omega c/(2U) = 0.1$ to compare lift coefficient histories (C_l vs. α) between experiments and CFD. The computational and experimental results are seen to compare well with each other, as shown in Fig. 6.

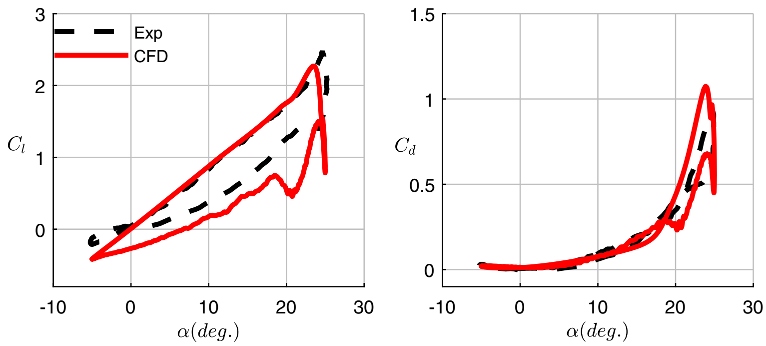

(a) (b)

Fig. 7 Comparison of computed C_l and C_d versus α with experimental results of Lee et al. [74] for the NACA 0012 airfoil at Re =1.35 × 10^5

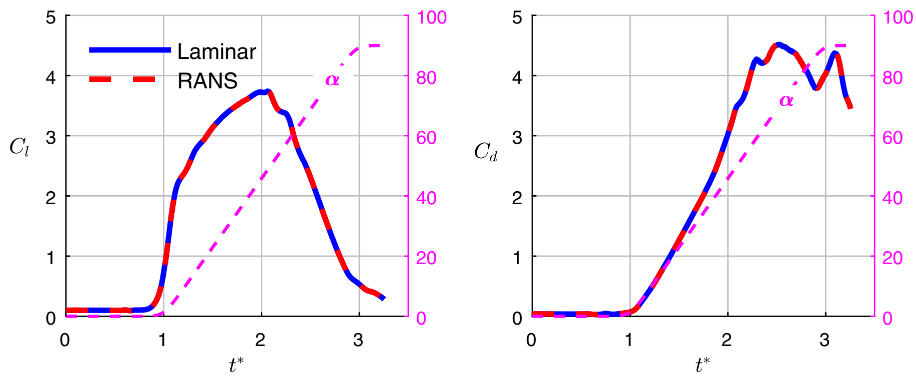

(a) (b)

Fig. 8 Comparison for the SD7003 airfoil undergoing a pitch-up and hold motion: computed C_l and C_d versus α between fully laminar and RANS results for Re = 10,000 and K = 0.4

Lee and Gerontakos [74] experimentally investigated the unsteady boundary layer and stall events occurring on a sinusoidally pitching NACA 0012 airfoil at $Re = 1.35 \times 10^5$. The pitching motion is given by $\alpha(t) = 10 + 15\sin(\omega t)$, with $k = 0.1$. The measured lift and drag coefficients, C_l and C_d, respectively, are used here to compare with REACTMB-INS predictions. As shown in Fig. 7, good agreement is observed between the measured data and the REACTMB predictions.

The current study is focused on a low Reynolds number of 10,000. At these Reynolds numbers, it is known that the boundary layer is mostly laminar over the airfoil and especially at the leading edge. To examine the difference between using a fully laminar-flow CFD solution and a CFD solution using a Reynolds-averaged Navier Stokes (RANS) model, the REACTMB-INS code was used with both these options for the analysis of a SD7003 airfoil undergoing a pitch-up–hold motion. The Spalart–Allmaras (SA) turbulence model was used for the RANS simulation. Figure 8 shows the results for the variations of C_l and C_d with convective time, $t^* = tU/c$, from the two simulations. It is seen that the results are essentially identical. An examination of the flow field from the RANS simulation confirmed that, for this Reynolds number, the solver activated the turbulence model only in the wake behind the airfoil and the boundary layer was laminar. Based on this analysis, it is seen that the choice of fully laminar vs. the use of a RANS turbulence model option in the CFD analysis does not matter for the Reynolds numbers considered in this work. All the simulations in this paper are carried out using the RANS model with the SA turbulence model.

4.3 Boundary-layer extraction algorithm

As an important part of the current work, we extract boundary-layer information from unsteady RANS computations for a large number of unsteady motions. According to conventional boundary-layer methodology, the height above the surface at which the surface-parallel component of the flow velocity is $0.99U_\infty$, where U_∞

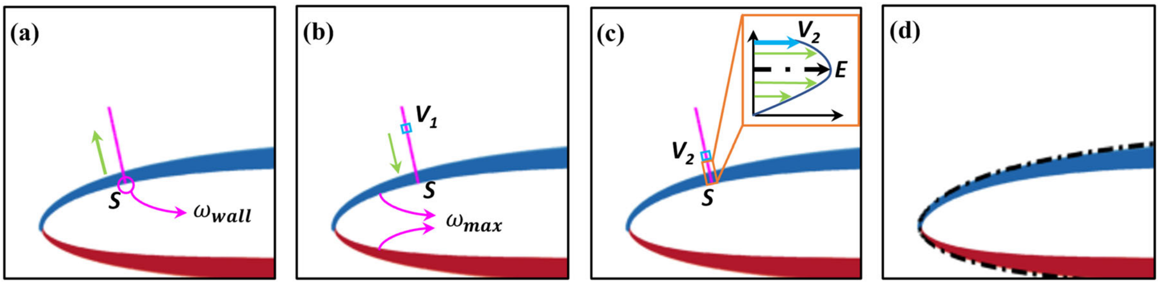

Fig. 9 Illustration of the steps used in the extraction of boundary-layer information from CFD

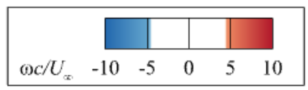

Fig. 10 Color bar for the non-dimensional vorticity ($\omega c / U_\infty$) contours for the CFD flow field plots presented in this paper

is the freestream velocity, is to be deemed as the edge of the boundary layer. This holds true only for flat-plate boundary layers. On an airfoil surface, because the edge velocity (U_e) could be greater than or less than U_∞, the conventional approach does not work, and an alternate approach needs to be developed. Since boundary layers can be viewed as regions of appreciable vorticity [75], we have developed a multi-step criterion which uses field data from CFD, i.e., vorticity and tangential velocities, at each time step to extract boundary-layer properties from the CFD solution. Figure 9 illustrates the steps in the procedure using the color contour of the vorticity around the airfoil surface for a representative case. The color scale for this and all the following vorticity contour plots shown in his paper is shown in Fig. 10.

The boundary-layer extraction procedure uses the following steps:

1. The airfoil surface is first discretized into several points. At each point, a surface normal is constructed, and flow quantities (vorticity and velocity) are extracted at several points along the normal. The vorticity at the surface, ω_{wall}, is calculated for each point on the airfoil, as illustrated in Fig. 9a in which the surface point is labeled "S." The maximum surface vorticity, $\omega_{\max}$, is defined as the maximum of the vorticity at the wall over the entire airfoil surface (maximum value of ω_{wall} for all points on the airfoil) at a given time step or pitch angle and is also calculated and stored.
2. For each surface point, the vorticity values along the normal are examined to determine the location at which the vorticity ratio, $\omega/\omega_{\text{wall}}$, becomes negligible. (A value of 1×10^{-5} has been used in this work.) From our experience with a large number of cases, this location, labeled "V_1" in Fig. 9b, is the outer-most possible location for the boundary-layer edge.
3. In the next step, we traverse in the opposite direction along the normal from the location V_1 to S, as shown in Fig. 9b, to identify the location at which the ratio $\omega/\omega_{\max}$ approaches 1×10^{-3}. Based on our experience, this location denoted by "V_2," is a better approximation for the outer-most possible location for the boundary-layer edge. Using the ratio $\omega/\omega_{\max}$ for this step non-dimensionalizes the local vorticity with the maximum surface vorticity and makes the determination of V_2 in this step of the algorithm relatively insensitive to the flow conditions such as Reynolds number.
4. Next, we examine all the points on the normal line between the points V_2 and S to determine the point at which surface-parallel velocity is a maximum. As illustrated in Fig. 9c, this point, labeled "E," is taken as the edge of the boundary layer for this location on the airfoil. The procedure is then repeated at all surface points to estimate the boundary-layer edge around the airfoil as shown in Fig. 9d.

From the extracted velocity profile and the deduced boundary-layer thickness, δ, the displacement, momentum, and energy thicknesses, δ_1, δ_2, and δ_3, respectively, along with the shape factor, H_{32}, are calculated using Eqs. 12 – 15.

$$\delta_1 = \int_0^\delta \left(1 - \frac{u}{u_e}\right) \mathrm{d}y \tag{12}$$

$$\delta_2 = \int_0^\delta \frac{u}{u_e} \left(1 - \frac{u}{u_e}\right) \mathrm{d}y \tag{13}$$

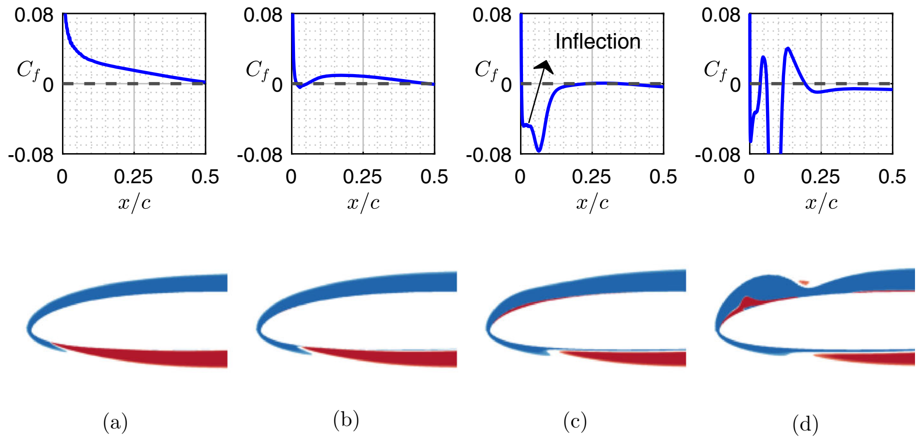

Fig. 11 Skin-friction plots and vorticity contours for α values during a pitch-up motion leading to LEV formation: **a** $\alpha = 18.4°$ **b** $\alpha = 23.4°$ **c** $\alpha = 28.5°$ **d** $\alpha = 33.5°$

$$\delta_3 = \int_0^{\delta} \frac{u}{u_e}\left[1 - \left(\frac{u}{u_e}\right)^2\right] \mathrm{d}y \tag{14}$$

$$H_{32} = \frac{\delta_3}{\delta_2} \tag{15}$$

4.4 Identification of LEV initiation from CFD results

An important aspect in the current work is to consistently identify the time instant of LEV initiation from CFD results. Although the initiation of LEV can qualitatively be inferred from the CFD flow field pictures by selecting the time at which the first sign of an LEV structure appears, it is desirable to have an approach that can be unambiguously applied to any motion case and that uses only surface quantities to allow for easy determination for a large number of cases. For this purpose, we have used the skin-friction signature, which is described in detail in Narsipur et al. [17]. This approach is explained by examining the events that lead to the formation of an LEV for an example pitch-up case. Figure 11 displays the upper-surface skin-friction coefficient, C_f, and the corresponding vorticity contours around the front half of the airfoil for four angles of attack: at $\alpha = 18.4$ degrees shown in Fig. 11a, at which the flow over the front portion of the airfoil is fully attached (C_f is positive); at $\alpha = 23.4$ degrees shown in Fig. 11b, at which the first onset of flow reversal is seen at the leading edge (C_f first becomes negative); at $\alpha = 28.5$ degrees shown in Fig. 11c, at which an inflection point first occurs in the negative-C_f region over which the surface flow is reversed; and at $\alpha = 33.5$ degrees shown in Fig. 11d, at which the vorticity contour shows the presence of an LEV structure in the early stage of its formation. The time instant corresponding to the C_f signature shown in Fig. 11c is used as the time corresponding to LEV initiation. While it is well known that the occurrence of negative C_f in unsteady flow does not indicate flow separation [40–45], we use the occurrence of negative C_f to indicate flow reversal, which is a consistent precursor to LEV initiation [2,3,30,59,76–78].

4.5 Flow-reversal behavior during pitch-up motion

In this section, detailed results from the CFD solution for the baseline case are used to examine the behavior of the surface and boundary-layer flow features as the pitch angle is increased. Of specific interest is the chordwise variation of the boundary-layer shape parameter, H_{32} (Eq. 15), which is known to reach a critical value at the location of flow reversal in steady laminar boundary layers.

It is well known that when a rounded-leading-edge airfoil is pitched up, the flow-separation behavior depends on the non-dimensional pitch rate (K). For small pitch rates (e.g., $K = 0.005$ for the SD7003 airfoil at Re = 10,000), reversed flow on the upper surface progresses upstream from the trailing edge with increasing pitch angle until it reaches the leading-edge region, leading to a massively separated flow on the airfoil without

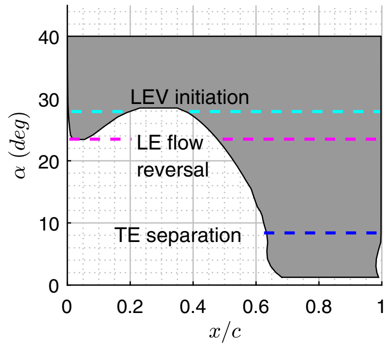

Fig. 12 Variation of upper-surface flow reversal for the baseline case

the formation of a distinct LEV. On the other hand, for higher pitch rates (K of ≈ 0.1 and higher for the SD7003 airfoil at $Re = 10,000$), although a trailing-edge flow-reversal zone starts at small pitch angles and progresses upstream with increasing pitch angle, a distinct region of flow reversal develops near the leading edge, which shortly thereafter gives rise to vortex shedding leading to LEV formation. This distinct region near the leading edge is caused by the adverse pressure gradient becoming high enough to cause flow reversal followed by vortex shedding. In earlier works, this behavior was shown to be associated with the LESP reaching a critical value. Because the current work focuses on LEV formation, the interest is on the flow features for such higher-pitch-rate motions. Figure 12 presents the variation of upper-surface flow-reversal regions (chordwise locations where $C_f \leq 0$) with pitch angle, α, for the baseline case. The chordwise regions of reversed flow at the surface are shaded in gray. For the three pitch angles marked in Fig. 12, Fig. 13 shows surface flow details: a zoomed-in plot of vorticity contours overlaid with streamlines, the upper-surface chordwise variations of C_f, and a plot of the H_{32} vs x/c. The vorticity contour plots are presented with the airfoil chord oriented along the horizontal direction.

Examining the results for $\alpha = 8.3°$ in Fig. 13a, it is seen that C_f is positive until $x/c = 0.6$ beyond which trailing-edge reversed flow occurs. This behavior is corroborated by the vorticity plot in which the streamlines confirm the upper-surface reversed flow near the trailing edge. The CFD-extracted H_{32} is seen to gradually decrease from approximately 1.6 in the leading-edge region to approximately 1.53 at $x/c = 0.6$, which is the location for the start of flow reversal. Aft of $x/c = 0.6$, the H_{32} rises sharply in the reversed-flow region, much of which is shown as a gray shaded region, with the dotted blue line showing the calculated variation of H_{32} in this region. For much of the flow-reversal region, the procedure for the calculation of H_{32} breaks down, resulting in artificially high values. This behavior is ignored in the current work, which is the reason for the gray shading in the H_{32} plots for these regions.

Next, looking at $\alpha = 23.4°$ in Fig. 13b, it is seen from the C_f plot that the start of the trailing-edge flow reversal has moved upstream to $x/c \approx 0.5$. More interestingly, it is seen that a second, distinct region of reversed flow near the leading edge has started to form at this pitch angle, as seen by the C_f becoming negative over a small chordwise extent near the leading edge. It is seen that the H_{32} reaches a minimum value of approximately 1.515 at the location near the leading edge where C_f becomes negative. The occurrence of the new and distinct region of reverse flow near the leading edge is also shown in Fig. 12 for this pitch angle.

For the pitch angle of 28.5°, Fig. 13c shows that the C_f remains negative for a larger region near the leading edge indicating that the region of reversed flow at the trailing edge has grown in size in comparison with that for α of 23.4°. The C_f distribution shows an inflection point in the negative-C_f region at the leading edge, which signals the initiation of LEV formation, which is indicated by the small bulge in the vorticity contours and streamlines at the leading edge. For this condition also, it is again seen that the H_{32} decreases to approximately 1.518 at the start of the reversed-flow region at the leading edge. This result shows that H_{32} reaches a value close to 1.515 at the location of the start of surface flow reversal, indicating that this behavior could be used to predict the occurrence of flow reversal even in unsteady airfoil flows. However, the H_{32} at the location of the occurrence of flow reversal is always around 1.515 even for higher pitch angles when the reversed-flow region has become larger. Because the calculation of H_{32} is not reliable in regions of separation, the criticality of H_{32} can be used to identify only the initial onset of reversed flow and cannot be used to characterize the subsequent development of events such as the initiation of LEV formation.

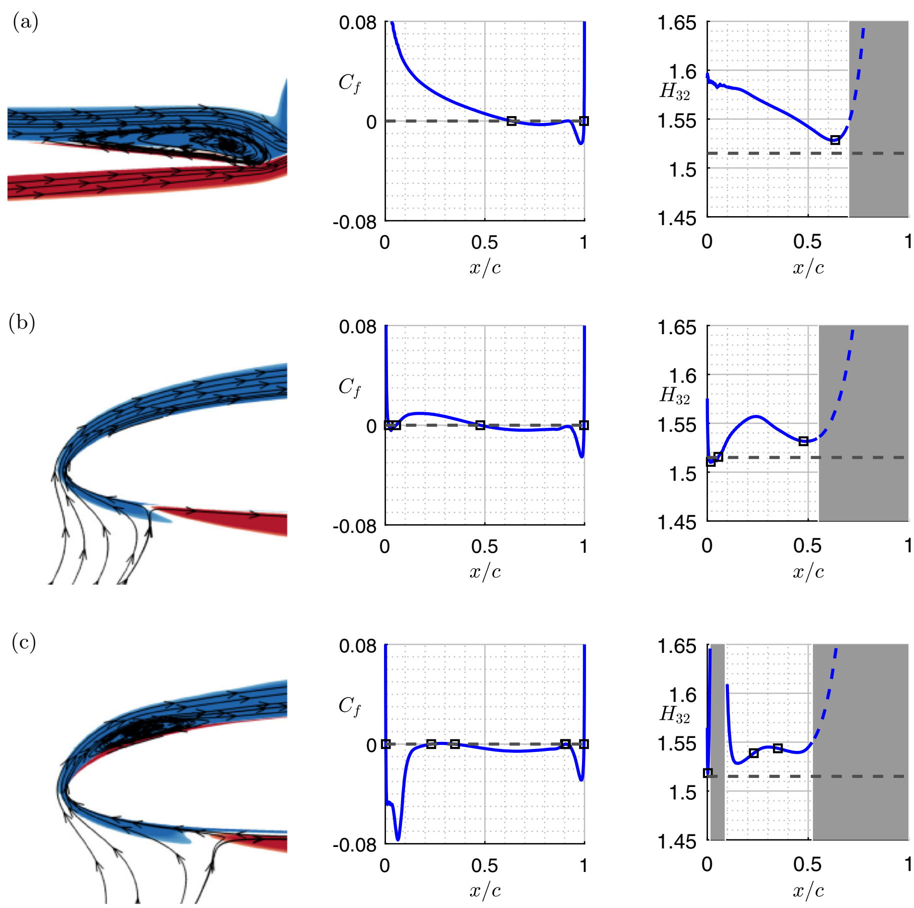

Fig. 13 Flow features for the baseline case at **a** α = 8.3 degrees, **b** α = 23.4 degrees, and **c** α = 28.5 degrees

4.6 Criticality of boundary-layer shape factor

To confirm the universality of H_{32} criticality, Fig. 14 plots the H_{32} values at the x/c locations corresponding to the start of the upper-surface leading-edge reversed-flow regions for each of the 9 cases listed in Table 1 for all pitch angles from the onset of flow reversal to the LEV initiation in each case. Also shown for reference are dashed lines corresponding to H_{32} values (for steady, incompressible flow) of 1.515 (purple) corresponding to laminar separation, 1.57 (red) corresponding to a flat-plate zero-pressure-gradient flow, and 1.62 (cyan) corresponding to stagnation-point flow. These values provide an appropriate scale for the H_{32} axis. It is seen that the H_{32} values for all these cases are clustered close to H_{32} of 1.515, indicating that criticality of H_{32} could be used to identify the onset of flow reversal for unsteady airfoil motions for the range of pitch rates, pivot locations, Reynolds numbers, and leading-edge radii used in this study. This result provides the motivation for the development of a low-order approach to prediction of leading-edge flow reversal using computationally inexpensive methods, leading to the second part of the research effort described in the following section.

5 Low-order prediction methodology

The low-order method (LOM) used in this work has two parts: (i) the unsteady vortex panel method (UVPM), described in Sect. 5.1, and (ii) the integral-boundary-layer method (IBL), described in Sect. 5.2. The combined LOM is described in Sect. 5.3. The LOM results for an example case are compared with CFD results in Sect. 5.4.

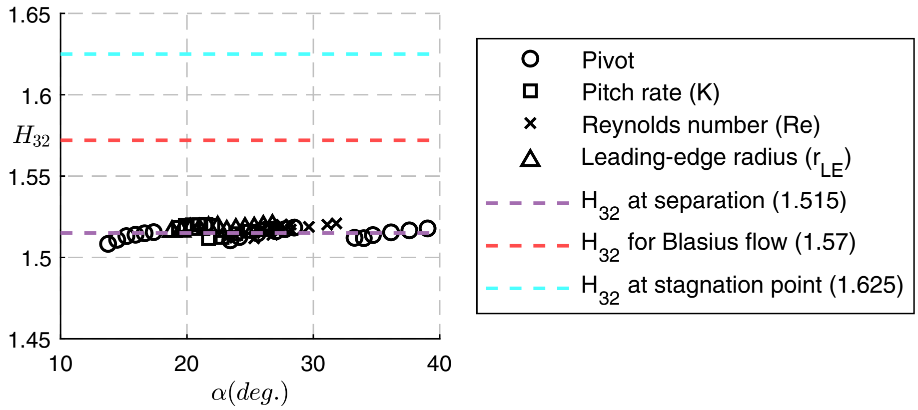

Fig. 14 Shape factor (H_{32}) at the occurrence of leading-edge reversal for all cases listed in Table 1

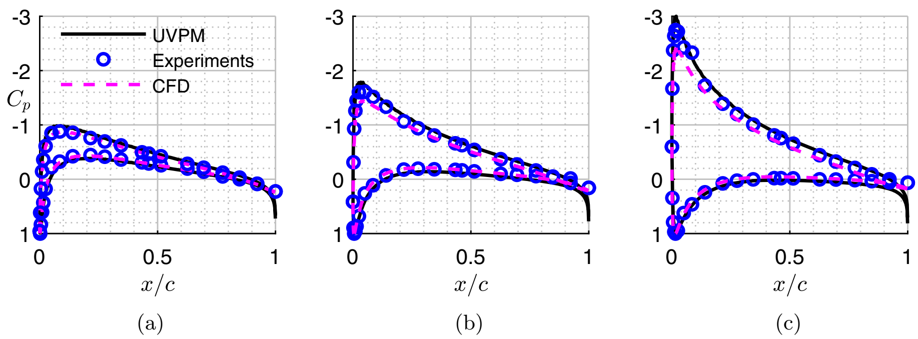

Fig. 15 C_p comparisons with the experiments of Müller-Vahl et al. [82] for a sinusoidally pitching NACA 0018 airfoil pivoted about the quarter chord **a** $\alpha = 2.1°$ **b** $\alpha = 5.9°$ **c** $\alpha = 9.3°$ during pitch up

5.1 Unsteady vortex panel method

Panel methods have been extensively used in the past to analyze flows past bodies of realistic geometries and have proved to be successful under certain circumstances. It is important to understand that these methods are based on potential-flow solutions and hence their forte is in accurately solving attached flow fields. The use of these dates back to Hess and Smith [79]. Several extensions of these have been developed for many flow situations. In the current method, we adopt an unsteady vortex panel method from Katz and Plotkin [80], as implemented by Young [81], for calculating the potential-flow pressure distribution on pitching airfoils.

5.1.1 Validation of the UVPM

Three sets of comparisons were performed to establish the accuracy of the UVPM. In the first set of comparisons, experimental results from Müller-Vahl et al. [82] for a sinusoidal pitching NACA 0018 airfoil at a freestream Reynolds number of 0.37 million are compared with the computed coefficient of pressure (C_p) from CFD and UVPM. The plots show excellent agreement between all three data sets as shown in Fig. 15. The comparisons have been carried out only for small angles of attack at which viscous effects are relatively small.

In the next set of comparisons, we compared the velocity distributions for an SD7003 airfoil between UVPM and CFD results from the current work for two pitch rates. Figure 16 shows that the velocity distributions for $K = 0.4$, plotted against arc length from the upper-surface trailing edge to the lower-surface trailing edge, obtained from UVPM display very good agreement with CFD. Overall, the stagnation points between the two formulations match each other across various angle of attacks. For the higher α case, it is seen that the non-dimensional boundary-layer edge velocity, U_e/U_∞, is slightly higher in the UVPM formulation compared to CFD. The reduced suction in the CFD results from the decambering effect of thick boundary layers and trailing-edge separation. Similar behavior is seen for the velocity comparisons for $K = 0.1$ as shown in Fig. 17.

In the last set, we looked at $\mathcal{L}$ and flowfield comparisons between CFD, UVPM, and the LDVM low-order method developed by Ramesh et al. [16]. The baseline case (from Table 1) has been chosen for comparison.

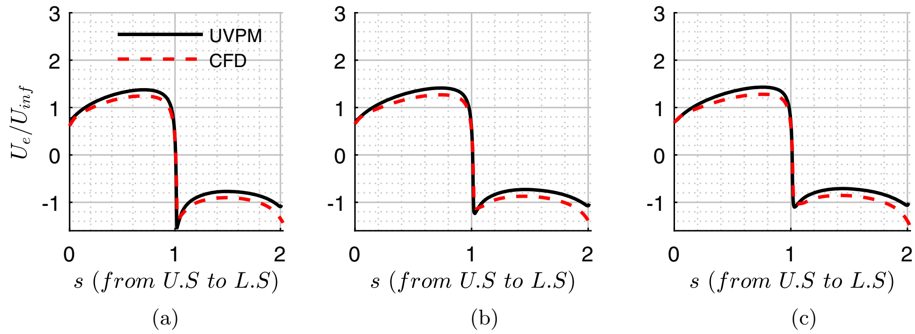

Fig. 16 Velocity distributions plotted against airfoil arc length, s, for K = 0.4, half-chord pivot (L-R) **a** $\alpha = 6.07°$ **b** $\alpha = 8.73°$ **c** $\alpha = 10.10°$

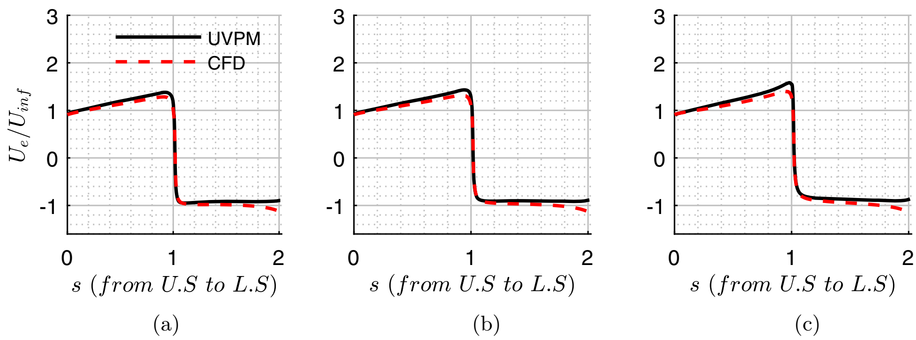

Fig. 17 Velocity distributions plotted against airfoil arc length, s, for K = 0.1, half-chord pivot (L-R) **a** $\alpha = 6.33°$ **b** $\alpha = 7.41°$ **c** $\alpha = 9.58°$

Because the UVPM has no model for LEV shedding, the LEV shedding has been turned off in LDVM as well to ensure an equitable comparison between the two formulations. The variation of $\mathcal{L}$ obtained from LDVM is the A_0 Fourier coefficient of the bound-vortex-sheet distribution, while the $\mathcal{L}$ obtained in UVPM and CFD is calculated by integrating C_p distributions over the airfoil from the leading-edge to the predefined $(x/c)_{max}$, as discussed in Sect. 2.3. The $\mathcal{L}$ comparison is shown in Fig. 18a. Comparing the time variations from the two low-order methods first, it is seen that the UVPM-predicted $\mathcal{L}$ is higher than that predicted by LDVM. This difference is because the UVPM predicts thickness effects, whereas the LDVM, being a thin-airfoil formulation, does not model thickness effects. Comparing the LDVM prediction with that from CFD next, it is seen that, until the onset of LEV initiation at $t^* = 1.62$, the LDVM and CFD time variations have roughly the same trend with the LDVM $\mathcal{L}$ being slightly higher than that of the CFD due to the absence of the reduction in suction caused by the viscous "decambering effects" in the CFD predictions. After LEV initiation, the $\mathcal{L}$ predicted by CFD levels off due to the LEV formation. In Fig. 18b, the shapes of the trailing-edge-vortex wakes are compared at $t^* = 1.26$ (marked in Fig. 18a) and have good similarity with each other. The wake roll-up and locations of the previously shed vortices are in good agreement between the three approaches.

5.2 Integral boundary layer

The use of the steady integral-boundary-layer calculation keeps the low-order method (LOM) numerically simpler compared to a relatively more intensive unsteady boundary-layer method. In our current work, we are focused on events preceding the onset of flow reversal at the leading edge when the flow at the leading-edge is attached. The method in this work, currently limited to handling only laminar boundary layers, is an adaptation of that presented by Selig and Maughmer [37]. It uses steady boundary-layer closure relations from Drela and Giles [36] using the instantaneous velocity distribution from the UVPM as input. The steady boundary layer closure relations are provided below.

$$H_{32} = 1.515 + 0.076\frac{(4 - H_{12})^2}{H_{12}}, \quad H_{12} < 4$$

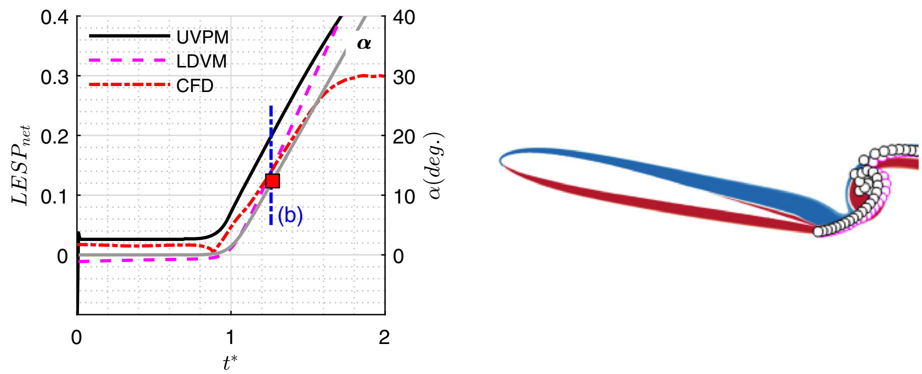

(a) (b)

Fig. 18 Baseline case: **a** $\mathcal{L}$ versus t^* **b** Comparison of flow features between CFD, UVPM (black), and LDVM (pink) at $t^* = 1.26$ (color figure online)

$$= 1.515 + 0.040 \frac{(H_{12} - 4)^2}{H_{12}}, \quad H_{12} > 4 \tag{16}$$

$$\mathrm{Re}_{\delta_2} \frac{C_f}{2} = -0.067 + 0.01977 \frac{(7.4 - H_{12})^2}{H_{12} - 1}, \quad H_{12} < 7.4$$

$$= -0.067 + 0.022 \left(1 - \frac{1.4}{H_{12} - 6}\right)^2, \quad H_{12} > 7.4 \tag{17}$$

$$\mathrm{Re}_{\delta_2} \frac{2C_D}{H_{32}} = 0.207 + 0.00205\,(4 - H_{12})^{5.5}, \quad H_{12} < 4$$

$$= 0.207 - 0.003 \frac{(H_{12} - 4)^2}{\left(1 + 0.02\,(H_{12} - 4)^2\right)}, \quad H_{12} > 4 \tag{18}$$

Using the results from UVPM and IBL, the first occurrence of reversed flow near the leading-edge region is determined by identifying the time instant when H_{32} first approaches the critical value of 1.515 in this region.

5.3 Low-order boundary-layer prediction methodology

The low-order prediction approach here combines the UVPM and the IBL. To calculate the upper-surface boundary layer at any instant of time for an unsteady motion, the UVPM-predicted instantaneous upper-surface velocity distribution from the stagnation point is used as input to the IBL. The IBL calculates the boundary-layer development until the occurrence of flow reversal (identified by $H_{32} = 1.515$). This IBL method does not have the capability to calculate the boundary-layer properties at chordwise locations much beyond this first occurrence of flow reversal. Future improvement could examine the use of an unsteady boundary-layer calculation approach like that presented in Matsushita et al. [46,47] and Paturle et al. [48] which has the capability to continue the calculation beyond the first occurrence of flow reversal until the location of unsteady separation. The main objective of this low-order prediction approach in this work is to identify the time instant of the onset of flow reversal at the leading edge, which has been shown to be a precursor to initiation of LEV formation.

To illustrate this calculation approach, the upper-surface H_{32} variations from this low-order prediction approach are presented for the baseline motion for a series of pitch angles in Fig. 19a. For comparison, Fig. 19b shows the upper-surface C_f variations for several pitch angles extracted from the CFD using the method described in Sect. 4.3. It is seen that at small pitch angles, in both CFD and low-order predictions, the airfoil has upper-surface reversed flow near the trailing-edge region. The occurrence of reversed flow is signaled in the CFD results by C_f crossing from positive to negative, and in the low-order results by H_{32} crossing from > 1.515 to < 1.515. With increasing pitch angle, the chordwise location for the first occurrence of reversed flow is seen to progressively move to smaller x/c values. At some pitch angle, both sets of results show the development of a minimum in the leading-edge region resulting from the leading-edge adverse pressure

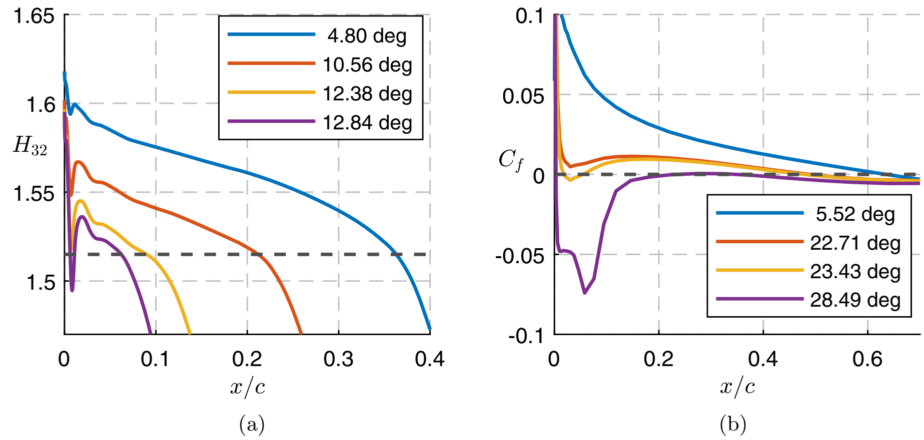

Fig. 19 Identification of the onset of flow reversal at the leading edge using **a** LOM and **b** CFD

gradient causing the boundary-layer to tend toward flow separation. At some pitch angle (the value of which is different between the CFD and low-order predictions), this minimum crosses the critical value (of $C_f = 0$ in the CFD results and $H_{32} = 1.515$ in the low-order results) indicating the sudden onset of flow reversal at the leading edge, resulting in a rapid movement of the chordwise location of the occurrence of flow reversal. The time instant corresponding to the sudden crossing over across the critical value is taken as the onset of leading-edge flow reversal. Although the low-order approach is incapable of predicting the LEV initiation, which occurs shortly after the onset of flow reversal, CFD results can be used to determine this time instant using the inflection point in the C_f distribution as described earlier in Sect. 4.4.

5.4 CFD versus low-order prediction for the baseline case

In this subsection, we compare the LOM and CFD predictions for the baseline case. Figure 20a compares the variation of the LESP with pitch angle from CFD and UVPM predictions, and Fig. 20b compares the variation of x/c for the first occurrence of flow reversal with $\mathcal{L}$ between CFD and LOM. In both these plots, the triangle symbols show the conditions corresponding to the CFD and LOM curves plotted in Fig. 19. The $\mathcal{L}$ at any pitch angle from CFD and UVPM has been calculated by integration of the corresponding pressure data over the leading-edge region, as described in Sect. 2.3. It is seen that the UVPM predicts a higher $\mathcal{L}$ than CFD. This is because of the decambering effect of the thick and separated boundary layers on the aft portion of the upper surface in CFD, which results in a reduction of the suction peak at the leading edge. On the other hand, the potential-flow model in UVPM, which does not have any effective shape change due to the boundary layer, predicts a higher suction peak. This difference in the suction peak between CFD and UVPM is also shown earlier in Figs. 16 and 17.

Next, we compare the predicted variations of the location of the first occurrence of flow reversal on the upper surface from CFD and LOM in Fig. 20b. This variation has been plotted with $\mathcal{L}$ on the vertical axis. The advantage of using the $\mathcal{L}$ instead of α for the vertical axis to compare the CFD and low-order predictions is that the $\mathcal{L}$ takes the amount of leading-edge suction (for each α from each method) into consideration. As a result, the discrepancy between the two curves is smaller when plotted against $\mathcal{L}$ instead of against α.

Examining the CFD result first, it is seen that even at small pitch angles, there is flow reversal starting from approximately $x/c = 0.7$ due to trailing-edge separation. With increasing pitch angle, this x/c value moves forward until LESP = 0.23 ($\alpha = 23$ degrees), when it jumps forward due to the sudden onset of flow reversal at the leading edge. At a slightly higher pitch angle of 28.5 degrees, when LESP = 0.27, CFD predicts the initiation of LEV formation. Examining the LOM prediction, it is seen that, at the low $\mathcal{L}$ values, the predicted x/c for flow reversal is smaller than that from the CFD results, indicating earlier occurrence of flow reversal in the UVPM. This discrepancy is attributed to the higher suction peak and greater adverse pressure gradients predicted in the potential-flow UVPM compared to the viscous CFD results that account for the thick and separated boundary layers. The UVPM variation, like the CFD result, also shows a sudden forward movement of the x/c for flow reversal, which is less abrupt than the corresponding jump seen in the CFD result, and occurs at a smaller $\mathcal{L}$ of 0.20, corresponding to $\alpha = 12.4$. This $\mathcal{L}$ value is taken as the LOM prediction for the

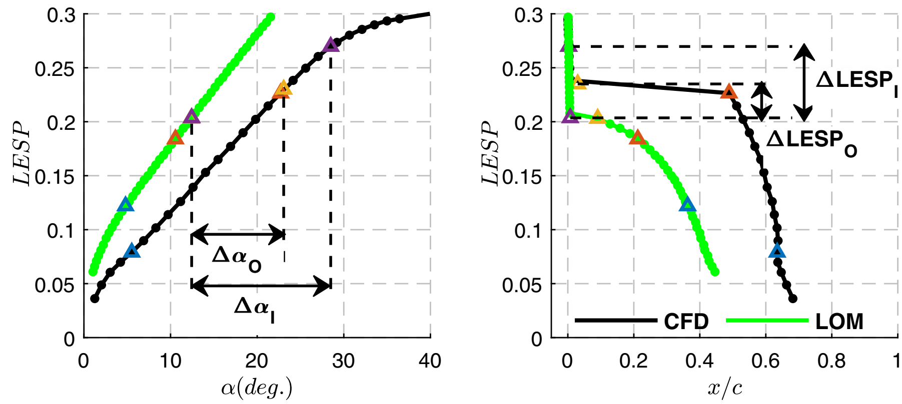

(a) (b)

Fig. 20 CFD and LOM predictions for the baseline case

onset of flow reversal. If the LOM predicted α and $\mathcal{L}$ for the first onset of flow reversal at the leading edge are taken as the reference values, it is seen that the CFD-predicted onset of flow reversal at the leading edge is delayed by a $\Delta\alpha_O$ of 10.6 degrees or a $\Delta\mathrm{LESP_O}$ of 0.026, and the CFD-predicted LEV initiation is delayed by a $\Delta\alpha_I$ of 16 degrees or a $\Delta\mathcal{L}_I$ of 0.066. If the LOM is to be used for rapid prediction of leading-edge flow reversal and LEV initiation for a range of motion parameters and airfoil shapes without the benefit of CFD results, then these empirically determined offsets between the LOM and CFD predictions for this case should be mostly independent of motion parameters and airfoil shapes. In the following section, the results for all the cases are examined to assess whether the low-order prediction with such an empirical offset can be used to predict LEV initiation for multiple motions and airfoils.

6 Results

We first present the results for all the motion cases for the SD7003 airfoil in Sect. 6.1. These results are also used to assess the empirically determined offsets in α and $\mathcal{L}$ between the CFD and LOM predictions for the baseline case in Sect. 5.4. The next subsection (Sect. 6.2) presents results for a different airfoil (NACA 0012) and compares the LOM predicted results corrected using the same offsets determined for the SD7003 airfoil in Sect. 5.4 with the CFD results for the NACA 0012.

6.1 Results for the SD7003 airfoil

The LOM predictions for onset of flow reversal are compared with the CFD results for onset of flow reversal and LEV initiation for the nine SD7003-airfoil cases listed in Table 1. The results are presented in Fig. 21 for the four cases studies plotted in the four corresponding columns: pivot (x_p/c), pitch rate (K), leading-edge radius (r_{LE}), and Reynolds number (Re). In each column, the top row presents the comparison for the pitch angles, and the bottom row presents the results for the LESP values.

Examining the first column for the effect of pivot location, we see from the results plotted in the top row that the LOM-predicted pitch angle for the onset of flow reversal increases by almost 15 degrees as the pivot location is changed from the leading edge ($x_p/c = 0$) to the half-chord location ($x_p/c = 0.5$). The trend, which is as expected, is because of the effect of the increased motion-induced downwash at the leading edge as pivot is moved aft. This trend is also seen in the CFD results for both the onset of flow reversal and LEV initiation, except that the CFD results have an offset in the α values in comparison with the LOM predictions. Examining the results for $\mathcal{L}$ in the bottom row, it is seen that the LOM-predicted $\mathcal{L}$ values for onset of flow reversal vary by approximately 0.04 for pivot change from the leading-edge to the half-chord location. This trend is similar to those seen for the CFD-predicted $\mathcal{L}$ for onset of flow reversal and LEV initiation. Although the critical $\mathcal{L}$ is expected to be mostly invariant with pivot location, these trends in $\mathcal{L}$ values do show that there is a variation. However, the variation is relatively small, and the trends are nearly the same between LOM and CFD.

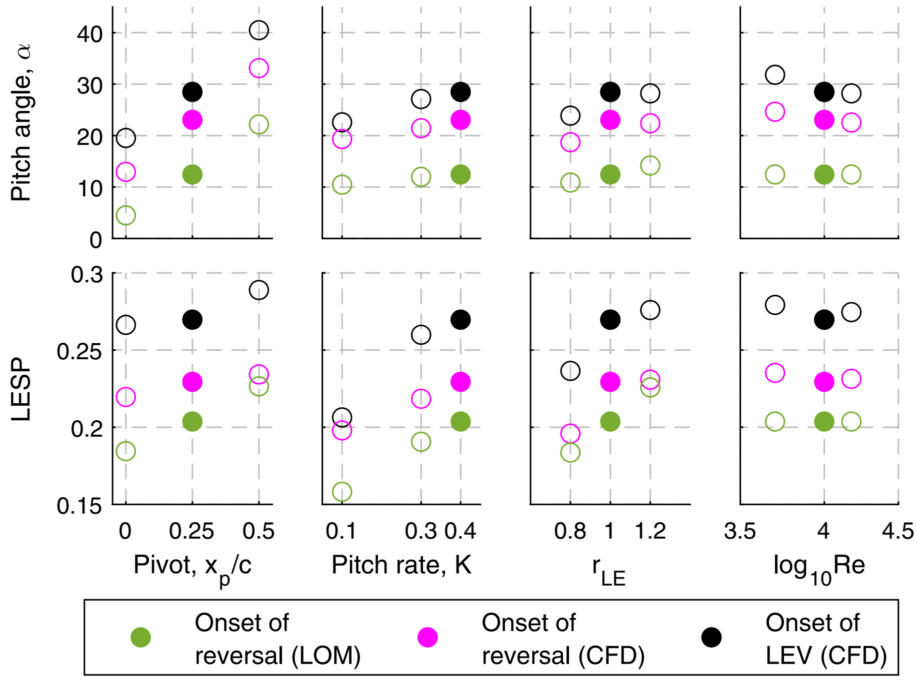

Fig. 21 Scatter plots showing the variations of LOM and CFD predictions for the SD 7003 airfoil. Baseline values are shown using filled symbols

Examining the data for the effect of non-dimensional pitch rate, K, on the pitch angle, α, in the upper row of the second column, the values of LOM-predicted α for onset of flow reversal are seen to be relatively invariant. Similar trends are seen in the CFD results as well. The $\mathcal{L}$ variations, plotted in the bottom row, from LOM and CFD predictions are similar in trend and show a change of approximately 0.05 for K variation from 0.1 to 0.4.

The plots in the third column show the effect of change in leading-edge radius, r_{LE}. Examining the trends in the top row, the changes in pitch angle due to the change in r_{LE} are seen to be relatively small, and the trends are similar between LOM and CFD. The variations of $\mathcal{L}$ in the bottom row show that there is an approximately 0.05 change in the $\mathcal{L}$ for both the CFD and LOM predictions over the range of r_{LE} studied here. It should be mentioned that critical $\mathcal{L}$ is not expected to be constant with change in r_{LE}, and an increase in the critical $\mathcal{L}$ is to be expected as the leading edge is made more round.

The fourth column shows the effect of Reynolds number. Examining the LOM results first, it is seen that the Reynolds number has no effect on the critical $\mathcal{L}$. This can be explained by noting that from theory, for a given pressure distribution, the location of laminar separation is invariant with Reynolds number. Examining the CFD results next, it is seen that Reynolds number has a small, but noticeable, effect on the critical $\mathcal{L}$. This behavior is attributed to the effect of the displacement thickness of the leading-edge boundary layer on the flow curvature of the outer-flow streamlines (the streamlines outside the boundary layer). The curvature of the leading-edge flow determines the leading-edge suction and, in turn, affects both the $\mathcal{L}$ and the tendency of the boundary layer to separate. Because the displacement thickness is affected by Reynolds number, there is an effect of Reynolds number on the critical $\mathcal{L}$. The results from the fourth column show that, for the range of Reynolds numbers considered here, the trends in the CFD results are still similar to those seen in the LOM results. For a larger Reynolds-number range, the deviation between LOM and CFD trends may become unacceptably high. Future work could examine the use of viscous–inviscid interaction in the low-order formulation to account for the effects of displacement thickness and bring the LOM trends closer to those seen from the CFD results.

One of the main aims of this work is to develop a low-order prediction method that uses boundary-layer criticality to predict onset of flow reversal and LEV initiation for a large range of motion parameters. Although the results of Fig. 21 show that the CFD results do not match with LOM predictions, it is seen that the trends matched well. To better compare these results from the viewpoint of the assessment of the LOM for predictive purposes, Fig. 22 plots the α and $\mathcal{L}$ results from CFD against the corresponding predictions from LOM for all the nine cases in Table 1. Figure 22a compares the CFD-predicted α values for onset of leading-edge flow

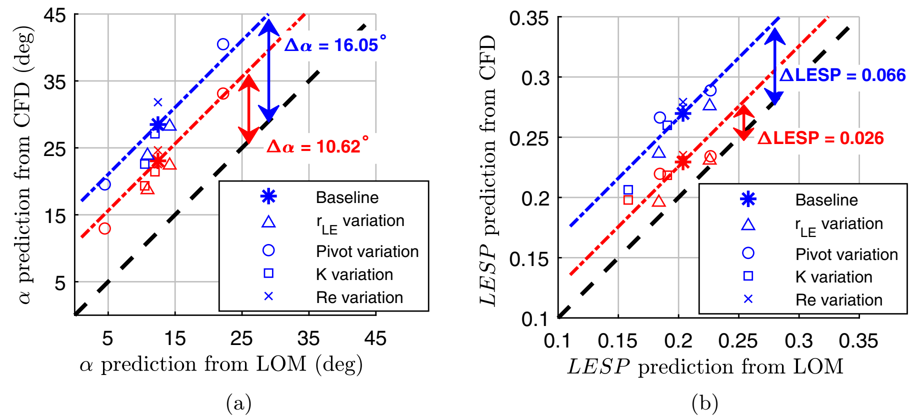

Fig. 22 CFD versus LOM predictions of pitch angle (α) and $\mathcal{L}$ for the nine cases with the SD 7003 airfoil

reversal and LEV initiation against the LOM-predicted α values for onset of leading-edge flow reversal. A 45-degree line is shown for reference to indicate the deviation of the results from a perfect 1:1 correlation. It is seen that the CFD results for the onset of flow reversal (red symbols) are all clustered around a 45-degree line that is offset from the perfect correlation line by the $\Delta\alpha_O$ of 10.6 degrees determined for the baseline case in Sect. 5.4. For all the cases considered here, the maximum α error from this offset line is 2.78 degrees. The CFD results for the LEV initiation (blue symbols) are also clustered around another 45-degree line that is offset from the perfect correlation line by the $\Delta\alpha_I$ of 16 degrees, with the maximum error being 3.9 degrees. These α offsets, determined for the baseline case, were listed in Sect. 5.4. Similar results are shown in Fig. 22b, which plots the CFD-predicted $\mathcal{L}$ values for onset of flow reversal and LEV initiation against the LOM-predicted $\mathcal{L}$ values for onset of flow reversal. Here too the CFD predictions are seen to be clustered around offset 45-degree lines, with the offsets, $\mathcal{L}_O$ and $\mathcal{L}_I$ obtained from the results for the baseline motion in Sect. 5.4. The maximum $\mathcal{L}$ error for flow-reversal onset from the corresponding offset 45-degree line is 0.020, and the maximum error for the LEV initiation from the corresponding line is 0.018. These results show that, with an empirical correction obtained for one motion, the corrected LOM prediction is able to predict either onset of leading-edge flow reversal or LEV initiation for any other motion within an acceptable error. As noted earlier, this empirical correction may work only for a limited Reynolds number range such as that used in this work. To expand the applicability over a larger range of Reynolds numbers may require enhancements to the LOM to incorporate the effect of displacement thickness.

6.2 Assessment of the LOM predictions for the NACA 0012 airfoil

It is of interest to assess the performance of the corrected LOM predictions, using the corrections empirically determined from the SD 7003 airfoil results, for another airfoil. Toward this objective, this section compares the prediction accuracy of the corrected LOM results with the CFD results for LEV initiation for the NACA 0012 airfoil. To obtain the LOM predictions, for each motion, the LOM (UVPM and IBL) was used to determine the α and $\mathcal{L}$ for the time instant corresponding to the first onset of flow reversal at the leading edge. These values were then corrected by adding the empirical offsets of $\Delta\alpha$ of 16 degrees and $\Delta LESP$ of 0.066 from Sect. 5.4 (determined from the results for the baseline motion for the SD7003 airfoil). Figure 23 shows the comparison of the CFD predictions for α and $\mathcal{L}$ for LEV initiation against the corrected LOM results for the nine motions. It is seen that the results are clustered around the 45-degree line for perfect correlation with the maximum error in α of 3.1 degrees and maximum error in $\mathcal{L}$ of 0.025. This excellent comparison shows the prediction effectiveness of the LOM not only for different motions, leading-edge shapes, and Reynolds numbers (within the limited range used in this work), but also for different airfoils.

7 Conclusions

Unsteady airfoil flows are often characterized by LEV formation and shedding. The growth and advection of the resulting LEV strongly affect the forces and moments on the airfoil and dominate the flowfield. Low-order

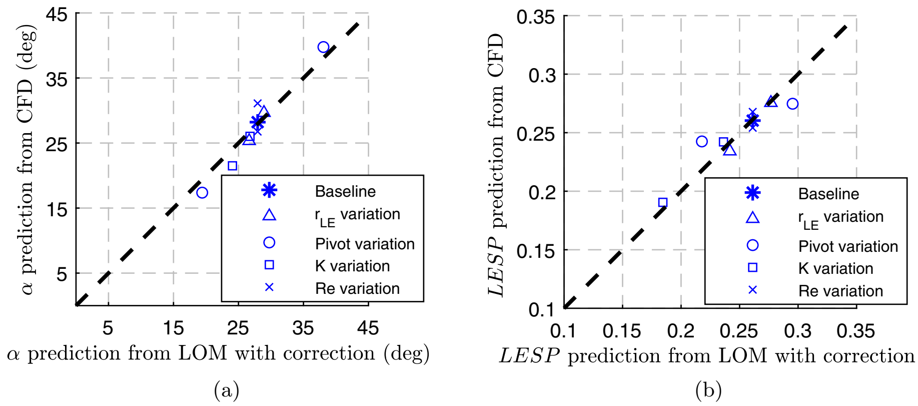

Fig. 23 CFD versus corrected LOM predictions of pitch angle (α) and $\mathcal{L}$ for the nine cases with the NACA 0012 airfoil

prediction of the initiation of LEV formation, however, has been a challenge, especially for round-leading-edge airfoil geometries. Recent works on the criticality of LESP as a governing factor for the initiation of LEV formation have shown success for both airfoil and finite-wing flows. The critical LESP, however, depends on both the leading-edge radius and the Reynolds number. As a result, for each new combination of leading-edge radius and Reynolds number, it needs to be determined using CFD or experiment for at least one motion case before it can be used for other motions. In this work, we propose that criticality of the boundary layer at the leading edge can be used as an improved governing criterion for predicting the initiation of LEV formation. To be used successfully in low-order predictions, one of the objectives of this work was that this boundary-layer criticality should be easily calculated using low-order approaches, thus avoiding the reliance on an expensive CFD or experimental result. With a focus on low Reynolds numbers at which the flow on the airfoil is fully laminar, the current work was carried out in two steps. In the first step, RANS CFD results were used to verify the hypothesis of boundary-layer criticality. In the second step, a low-order prediction approach was developed, in which an unsteady vortex panel method is used in combination with an integral-boundary-layer calculation to predict the occurrence of boundary-layer criticality at the leading edge. The results from the low-order approach are compared with the CFD results for LEV initiation.

To test the main hypothesis of boundary-layer criticality governing LEV initiation, in the first step, we examined RANS CFD results for a large set of pitch-up motions. The motions include systematic variations in pivot location, pitch rate, leading-edge radius, and Reynolds numbers. For each case, we extracted the boundary-layer information to determine the variation of the boundary-layer shape factor (H_{32}) from the stagnation point until the first occurrence of flow reversal on the upper surface of the airfoil. We show that the sudden occurrence of flow reversal at the leading edge is a precursor to LEV initiation, and this event is distinct from the slow forward-moving flow reversal that characterizes trailing-edge separation. For all the cases studied, it is shown that the value of the H_{32} at the onset of this leading-edge flow reversal is close to 1.515, which is the well-known critical value for flow separation in laminar boundary layers. This shape factor is not valid in separated regions, which prevents its use for characterizing the time instant of LEV initiation, which occurs shortly after the first onset of flow reversal. However, by consistently predicting the precursor event to LEV initiation, the results clearly support the hypothesis that criticality of boundary layer governs the initiation of LEV formation.

For the low-order prediction approach, an unsteady vortex panel method was used to obtain the instantaneous velocity distribution on the airfoil surface at a series of time steps in the motion. A steady integral-boundary-layer calculation was used to calculate the upper-surface boundary-layer development from the stagnation point until the first occurrence of flow reversal. Previous works have shown that a steady boundary-layer calculation is sufficient for such unsteady airfoil flows as long as the instantaneous surface velocity distribution is from an unsteady calculation. The occurrence of surface flow reversal is identified by the shape factor, H_{32}, reaching the previously determined critical value of 1.515. This boundary-layer method does not have the capability to continue the calculations beyond the first occurrence of flow reversal. During a pitch-up motion, a sudden forward movement of the flow-reversal location to the leading-edge region signifies the onset of leading-edge flow reversal. The predicted values of pitch angle and LESP for leading-edge flow-reversal onset for all the motions were compared against CFD results. Although the low-order predictions for flow reversal correctly captured the CFD trends in variation of pitch angle and LESP for LEV initiation with various motion parameters, they were offset from the CFD results. These pitch-angle and LESP offsets, attributed to the absence of viscous effects such as trailing-edge boundary-layer separation in the potential-flow panel method, were found to be mostly independent of the motion parameters. When these empirically determined offsets, calculated from the results for the baseline case of the SD 7003 airfoil, were applied to the low-order predictions for a different airfoil (NACA 0012), the results matched well with the CFD results with an error of ± 3 degrees in pitch angle and ± 0.025 in LESP. These results show the promise of this low-order approach. Future refinements to the approach could explore (i) the use of an unsteady boundary-layer method that can extend the calculation until the onset of flow separation, (ii) the use of viscous–inviscid interaction to account for displacement-thickness effects in the low-order calculations, and (iii) the extension of the approach to higher Reynolds numbers by using a transition model in the boundary-layer method.

Acknowledgements The authors would like to gratefully acknowledge Professor Jack Edwards of North Carolina State University (NCSU) for providing the REACTMB-INS code used for numerical results in this work. We also acknowledge the computing resources provided by North Carolina State University High Performance Computing Services Core Facility (RRID:SCR_022168).

Funding No funding was received for conducting this study.

Availability of data and materials The data that support the findings of this study are available from the corresponding author upon reasonable request.

Declarations

Conflict of interest The authors declare no competing financial interests.

Ethical approval Author A.G. is an Associate Editor for this journal.

Author contribution AG contributed to conceptualization, writing—review and editing, and supervision; HR and AG were involved in methodology and resources; HR contributed to formal analysis and investigation and writing—original draft preparation; and none contributed to funding acquisition.

References

1. McCroskey, W.J.: Unsteady airfoils. Annu. Rev. Fluid Mech. **14**(1), 285–311 (1982). https://doi.org/10.1146/annurev.fl.14.010182.001441
2. Ghosh Choudhuri, P., Knight, D., Visbal, M.R.: Two-dimensional unsteady leading-edge separation on a pitching airfoil. AIAA J. **32**(4), 673–681 (1994). https://doi.org/10.2514/3.12040
3. Ghosh Choudhuri, P., Knight, D.D.: Effects of compressibility, pitch rate, and Reynolds number on unsteady incipient leading-edge boundary layer separation over a pitching airfoil. J. Fluid Mech. **308**, 195–217 (1996). https://doi.org/10.1017/S0022112096001450
4. Widmann, A., Tropea, C.: Parameters influencing vortex growth and detachment on unsteady aerodynamic profiles. J. Fluid Mech. **773**, 432–459 (2015). https://doi.org/10.1017/jfm.2015.259
5. Benton, S.I., Visbal, M.R.: The onset of dynamic stall at a high, transitional Reynolds number. J. Fluid Mech. **861**, 860–885 (2019). https://doi.org/10.1017/jfm.2018.939
6. Li, Z.-Y., Feng, L.-H., Kissing, J., Tropea, C., Wang, J.-J.: Experimental investigation on the leading-edge vortex formation and detachment mechanism of a pitching and plunging plate. J. Fluid Mech. **901**, 17 (2020)
7. Kissing, J., Kriegseis, J., Li, Z., Feng, L., Hussong, J., Tropea, C.: Insights into leading edge vortex formation and detachment on a pitching and plunging flat plate. Exp. Fluids **61**(9), 208 (2020). https://doi.org/10.1007/s00348-020-03034-1
8. Jardin, T., Choi, J., Colonius, T.: An empirical correlation between lift and the properties of leading-edge vortices. Theoret. Comput. Fluid Dyn. **35**(4), 437–448 (2021). https://doi.org/10.1007/s00162-021-00567-x
9. Ōtomo, S., Henne, S., Mulleners, K., Ramesh, K., Viola, I.M.: Unsteady lift on a high-amplitude pitching aerofoil. Exp. Fluids **62**, 1–18 (2021)
10. Son, O., Gao, A.-K., Gursul, I., Cantwell, C.D., Wang, Z., Sherwin, S.J.: Leading-edge vortex dynamics on plunging airfoils and wings. J. Fluid Mech. (2022). https://doi.org/10.1017/jfm.2022.224
11. Seshadri, P.K., Aravind, A., De, A.: Leading edge vortex dynamics in airfoils: effect of pitching motion at large amplitudes. J. Fluids Struct. **116**, 103796 (2023)
12. Evans, W.T., Mort, K.W.: Analysis of computed flow parameters for a set of sudden stalls in low speed two-dimensional flow. Technical Report TN D-85, NACA (1959)
13. Beddoes, T.: Onset of leading edge separation effects under dynamic conditions and low mach number. In: American Helicopter Society, Annual National Forum, 34 Th, Washington, D. C, Proceedings, Research Supported by the Ministry of Defence,(Procurement Executive), vol. 15 (1978)
14. Ekaterinaris, J.A., Platzer, M.F.: Computational prediction of airfoil dynamic stall. Prog. Aerosp. Sci. **33**(11–12), 759–846 (1998). https://doi.org/10.1016/S0376-0421(97)00012-2
15. Morris, W.J., Rusak, Z.: Stall onset on aerofoils a low to moderately high Reynolds number flows. J. Fluid Mech. **733**, 439–472 (2013)

16. Ramesh, K., Gopalarathnam, A., Granlund, K., Ol, M.V., Edwards, J.R.: Discrete-vortex method with novel shedding criterion for unsteady airfoil flows with intermittent leading-edge vortex shedding. J. Fluid Mech. **751**, 500–538 (2014). https://doi.org/10.1017/jfm.2014.297
17. Narsipur, S., Hosangadi, P., Gopalarathnam, A., Edwards, J.R.: Variation of leading-edge suction during stall for unsteady aerofoil motions. J. Fluid Mech. **900**, 25 (2020). https://doi.org/10.1017/jfm.2020.467
18. Ham, N.D., Garelick, M.S.: Dynamic stall considerations in helicopter rotors. J. Am. Helicopter Soc. **13**(2), 49–55 (1968)
19. Crimi, P.: Dynamic stall. Technical report, Advisory Group for Aerospace Research and Development Paris (France) (1973)
20. McCroskey, W.J., McAlister, K., Carr, L., Pucci, S., Lambert, O., Indergrand, R.: Dynamic stall on advanced airfoil sections. J. Am. Helicopter Soc. **26**(3), 40–50 (1981)
21. Muijres, F.T., Johansson, L.C., Barfield, R., Wolf, M., Spedding, G.R., Hedenström, A.: Leading-edge vortex improves lift in slow-flying bats. Science **319**(5867), 1250–1253 (2008). https://doi.org/10.1126/science.1153019
22. Lentink, D., Dickson, W.B., Van Leeuwen, J.L., Dickinson, M.H.: Leading-edge vortices elevate lift of autorotating plant seeds. Science **324**(5933), 1438–1440 (2009)
23. Ford, C.W.P., Babinsky, H.: Lift and the leading-edge vortex. J. Fluid Mech. **720**, 280–313 (2013). https://doi.org/10.1017/jfm.2013.28
24. Videler, J., Stamhuis, E., Povel, G.: Leading-edge vortex lifts swifts. Science **306**(5703), 1960–1962 (2004)
25. Krishna, S., Green, M.A., Mulleners, K.: Flowfield and force evolution for a symmetric hovering flat-plate wing. AIAA J. **56**(4), 1360–1371 (2018)
26. Krishna, S., Green, M.A., Mulleners, K.: Effect of pitch on the flow behavior around a hovering wing. Exp. Fluids **60**(5), 1–17 (2019)
27. Liu, Z., Lai, J.C.S., Young, J., Tian, F.-B.: Discrete vortex method with flow separation corrections for flapping-foil power generators. AIAA J. **55**(2), 410–418 (2017). https://doi.org/10.2514/1.J055267
28. Hirato, Y., Shen, M., Gopalarathnam, A., Edwards, J.R.: Vortex-sheet representation of leading-edge vortex shedding from finite wings. J. Aircr. **56**(4), 1626–1640 (2019). https://doi.org/10.2514/1.C035124
29. Hirato, Y., Shen, M., Gopalarathnam, A., Edwards, J.R.: Flow criticality governs leading-edge-vortex initiation on finite wings in unsteady flow. J. Fluid Mech. **910**, 1 (2021). https://doi.org/10.1017/jfm.2020.896
30. Deparday, J., Mulleners, K.: Modeling the interplay between the shear layer and leading edge suction during dynamic stall. Phys. Fluids **31**(10), 107104 (2019). https://doi.org/10.1063/1.5121312
31. Smith, L.R., Jones, A.R.: Vortex formation on a pitching aerofoil at high surging amplitudes. J. Fluid Mech. **905**, 22 (2020). https://doi.org/10.1017/jfm.2020.741
32. Deparday, J., He, X., Eldredge, J.D., Mulleners, K., Williams, D.R.: Experimental quantification of unsteady leading-edge flow separation. J. Fluid Mech. **941**, 60 (2022). https://doi.org/10.1017/jfm.2022.319
33. Sudharsan, S., Ganapathysubramanian, B., Sharma, A.: A vorticity-based criterion to characterise leading edge dynamic stall onset. J. Fluid Mech. **935**, 10 (2022). https://doi.org/10.1017/jfm.2021.1149
34. Miotto, R., Wolf, W., Gaitonde, D., Visbal, M.: Analysis of the onset and evolution of a dynamic stall vortex on a periodic plunging aerofoil. J. Fluid Mech. (2022). https://doi.org/10.1017/jfm.2022.165
35. Eppler, R.A., Somers, D.M.: A computer program for the design and analysis of low-speed airfoils. Technical report, National Aeronautics and Space Administration, Scientific and Technical Information Branch (1980)
36. Drela, M., Giles, M.B.: Viscous-inviscid analysis of transonic and low reynolds number airfoils. AIAA J. (1987). https://doi.org/10.2514/3.9789
37. Selig, M.S., Maughmer, M.D.: Generalized multipoint inverse airfoil design. AIAA J. **30**(11), 2618–2625 (1992)
38. Gendrich, C.P.: Dynamic stall of rapidly pitching airfoils: MTV experiments and navier-stokes simulations. PhD thesis, Michigan State University (1999)
39. Prandtl, L.: Über flussigkeitsbewegung bei sehr kleiner reibung. Verhandl. III, Internat. Math.-Kong., Heidelberg, Teubner, Leipzig, pp. 484–491 (1904)
40. Rott, N.: Unsteady viscous flow in the vicinity of a stagnation point. Q. Appl. Math. **13**(4), 444–451 (1956)
41. Sears, W.: Some recent developments in airfoil theory. J. Aeronaut. Sci. **23**(5), 490–499 (1956)
42. Moore, F.K.: On the separation of the unsteady laminar boundary layer. In: Grenzschichtforschung/Boundary Layer Research, pp. 296–311 (1958)
43. Haller, G.: Exact theory of unsteady separation for two-dimensional flows. J. Fluid Mech. **512**, 257–311 (2004). https://doi.org/10.1017/S0022112004009929
44. Miron, P., Vétel, J.: Towards the detection of moving separation in unsteady flows. J. Fluid Mech. **779**, 819–841 (2015). https://doi.org/10.1017/jfm.2015.461
45. Klose, B.F., Jacobs, G.B., Serra, M.: Kinematics of Lagrangian flow separation in external aerodynamics. AIAA J. **58**(5), 1926–1938 (2020)
46. Matsushita, M., Murata, S., Akamatsu, T.: Studies on boundary-layer separation in unsteady flows using an integral method. J. Fluid Mech. **149**, 477–501 (1984). https://doi.org/10.1017/S0022112084002767
47. Matsushita, M., Akamatsu, T.: Numerical computation of unsteady laminar boundary layers with separation using one-parameter integral method: 2nd report, the separation singularity in unsteady boundary layer. Bull. JSME **28**(240), 1044–1049 (1985). https://doi.org/10.1299/jsme1958.28.1044
48. Paturle, M.L., Bose, C., Viola, I.M., Ramesh, K.K.: Dynamic detection of flow separation using integral formulation of unsteady boundary layer equations. In: AIAA Aviation 2022 Forum. American Institute of Aeronautics and Astronautics, Chicago, IL & Virtual (2022). https://doi.org/10.2514/6.2022-4138
49. McDonald, H., Shamroth, S.J.: An analysis and application of the time- dependent turbulent boundary-layer equations. AIAA J. **9**(8), 1553–1560 (1971). https://doi.org/10.2514/3.6391
50. Jones, K., Platzer, M.: On the prediction of dynamic stall onset on airfoils in low speed flow. In: Proceedings of the 8th International Symposium on Unsteady Aerodynamics and Aeroelasticity of Turbomachines, pp. 797–812 (1998)

51. Drela, M.: Newton solution of coupled viscous/inviscid multielement airfoil flows. In: 21st Fluid Dynamics, Plasma Dynamics and Lasers Conference. American Institute of Aeronautics and Astronautics, Seattle (1990). https://doi.org/10.2514/6.1990-1470
52. Narsipur, S., Gopalarathnam, A., Edwards, J.R.: Low-order modeling of airfoils with massively separated flow and leading-edge vortex shedding. In: 2018 AIAA Aerospace Sciences Meeting, pp. 0813 (2018)
53. Narsipur, S., Gopalarathnam, A., Edwards, J.R.: Low-order model for prediction of trailing-edge separation in unsteady flow. AIAA J. **57**(1), 191–207 (2019). https://doi.org/10.2514/1.J057132
54. Kamrani Fard, K., Ngo, V., Liburdy, J.A.: A leading-edge vortex initiation criteria for large amplitude foil oscillations using a discrete vortex model. Phys. Fluids **33**(11), 115123 (2021). https://doi.org/10.1063/5.0065097
55. Ramanathan, H., Narsipur, S., Gopalarathnam, A.: Boundary-layer characteristics at the onset of leading-edge vortex formation on unsteady airfoils. In: AIAA Aviation 2019 Forum. American Institute of Aeronautics and Astronautics, Dallas, Texas (2019). https://doi.org/10.2514/6.2019-3590
56. Ramanathan, H., Gopalarathnam, A.: Prediction of vortex initiation using an unsteady panel method with an integral-boundary-layer calculation. In: AIAA Aviation 2022 Forum. American Institute of Aeronautics and Astronautics, Chicago, IL & Virtual (2022). https://doi.org/10.2514/6.2022-3897
57. Ramesh, K.: On the leading-edge suction and stagnation-point location in unsteady flows past thin aerofoils. J. Fluid Mech. **886**, 13 (2020). https://doi.org/10.1017/jfm.2019.1070
58. Katz, J.: A discrete vortex method for the non-steady separated flow over an airfoil. J. Fluid Mech. **102**, 315–328 (1981)
59. Ramesh, K., Granlund, K., Ol, M.V., Gopalarathnam, A., Edwards, J.R.: Leading-edge flow criticality as a governing factor in leading-edge vortex initiation in unsteady airfoil flows. Theoret. Comput. Fluid Dyn. **32**(2), 109–136 (2018). https://doi.org/10.1007/s00162-017-0442-0
60. Kay, N.J., Richards, P.J., Sharma, R.N.: Low-Reynolds number behavior of the leading-edge suction parameter at low pitch rates. AIAA J. (2021). https://doi.org/10.2514/1.J060733
61. Ramesh, K., Gopalarathnam, A., Edwards, J.R., Ol, M.V., Granlund, K.: An unsteady airfoil theory applied to pitching motions validated against experiment and computation. Theoret. Comput. Fluid Dyn. **27**(6), 843–864 (2013). https://doi.org/10.1007/s00162-012-0292-8
62. Hirato, Y., Shen, M., Aggarwal, S., Gopalarathnam, A., Edwards, J.R.: Initiation of leading-edge-vortex formation on finite wings in unsteady flow. In: 53rd AIAA Aerospace Sciences Meeting. American Institute of Aeronautics and Astronautics, Kissimmee, Florida (2015). https://doi.org/10.2514/6.2015-0546
63. SureshBabu, A., Medina, A., Rockwood, M., Bryant, M., Gopalarathnam, A.: Theoretical and experimental investigation of an unsteady airfoil in the presence of external flow disturbances. J. Fluid Mech. **921**, 55 (2021). https://doi.org/10.1017/jfm.2021.484
64. Suresh Babu, A.V., Narsipur, S., Bryant, M., Gopalarathnam, A.: Leading-edge-vortex tailoring on unsteady airfoils using an inverse aerodynamic approach. Phys. Fluids **34**(5), 057107 (2022). https://doi.org/10.1063/5.0090328
65. Garrick, I.E.: Propulsion of a flapping and oscillating airfoil. Technical Report NACA TR 567, NACA (1937)
66. Drela, M.: Xfoil: an analysis and design system for low Reynolds number airfoils. In: Low Reynolds number aerodynamics, pp. 1–12 (1989)
67. Eldredge, J.D., Wang, C.J., Ol, M.V.: A computational study of a canonical pitch-up, pitch-down wing maneuver. In: AIAA Paper 2009–3687 (2009)
68. Granlund, K.O., Ol, M.V., Bernal, L.P.: Unsteady pitching flat plates. J. Fluid Mech. **733**, 5 (2013). https://doi.org/10.1017/jfm.2013.444
69. Cassidy, D.A., Edwards, J.R., Tian, M.: An investigation of interface-sharpening schemes for multiphase mixture flows. J. Comput. Phys. **228**(16), 5628–5649 (2009)
70. Colella, P., Woodward, P.R.: The piecewise parabolic method (ppm) for gas-dynamic simulations. J. Comput. Phys. **54**, 174–201 (1984)
71. Edwards, J.R., Chandra, S.: Comparison of eddy viscosity-transport turbulence models for three-dimensional, shock-separated flowfields. AIAA J. **34**(4), 756–763 (1996)
72. Nielsen, T.B., Edwards, J.R., Chelliah, H.K., Lieber, D., Geipel, C., Goyne, C.P., Rockwell, R.D., Cutler, A.D.: Hybrid large eddy simulation/reynolds-averaged navier-stokes analysis of a premixed ethylene-fueled dual-mode scramjet combustor. AIAA J. **59**(7), 2440–2456 (2021)
73. Leishman, J.G.: Dynamic stall experiments on the NACA 23012 aerofoil. Exp. Fluids **9**(1–2), 49–58 (1990). https://doi.org/10.1007/BF00575335
74. Lee, T., Gerontakos, P.: Investigation of flow over an oscillating airfoil. J. Fluid Mech. (2004). https://doi.org/10.1017/S0022112004009851
75. Tritton, D.J.: Physical fluid dynamics. Springer (2012). https://doi.org/10.1007/978-94-009-9992-3
76. Doligalski, T., Smith, C., Walker, J.: Vortex interactions with walls. Annu. Rev. Fluid Mech. **26**(1), 573–616 (1994)
77. Gupta, R., Ansell, P.J.: Unsteady flow physics of airfoil dynamic stall. AIAA J. **57**(1), 165–175 (2019). https://doi.org/10.2514/1.J057257
78. Le Fouest, S., Mulleners, K.: The dynamic stall dilemma for vertical-axis wind turbines. Renew. Energy **198**, 505–520 (2022). https://doi.org/10.1016/j.renene.2022.07.071
79. Hess, J.L., Smith, A.M.O.: Calculation of potential flow about arbitrary bodies. Prog. Aerosp. Sci. **8**, 1–138 (1967). https://doi.org/10.1016/0376-0421(67)90003-6
80. Katz, J., Plotkin, A.: Low-Speed Aerodynamics. Cambridge Aerospace Series, 2nd edn. Cambridge University Press, Cambridge (2001)
81. Young, J.: Numerical simulation of the unsteady aerodynamics of flapping airfoils. PhD thesis, University of New South Wales, Australian Defence Force Academy, School of Aerospace, Civil and Mechanical Engineering (2005)
82. Müller-Vahl, H.F., Strangfeld, C., Nayeri, C.N., Paschereit, C.O., Greenblatt, D.: Control of thick airfoil, deep dynamic stall using steady blowing. AIAA J. **53**(2), 277–295 (2015). https://doi.org/10.2514/1.J053090